

Landslides (2019) 16:2353–2367
 DOI 10.1007/s10346-019-01238-z
 Received: 10 January 2019
 Accepted: 4 July 2019
 Published online: 20 July 2019
 © Springer-Verlag GmbH Germany
 part of Springer Nature 2019

Guang Lu · Andrin Caviezel · Marc Christen · Sophia E. Demmel · Adrian Ringenbach · Yves Bühler · Claire E. Dinneen · Werner Gerber · Perry Bartelt

Modelling rockfall impact with scarring in compactable soils

Abstract An accurate modelling of rockfall runout continues to be a demanding challenge within the geotechnical and hazards engineering community. Most existing rockfall dynamic programs apply effective restitution coefficients to model the energy dissipation during the rock-ground interaction. Recent experimental measurements, however, reveal the limitations of effective restitution coefficients, especially to account for scarring with frictional rebound in soft compactable soils. This study proposes a three-dimensional, non-smooth computational mechanic approach to model dissipative rock-ground interactions in soft compactable soils. The ground is mathematically divided into a soft, compactable scarring layer and a hard rebound layer. The model considers the plastic deformation of the ground with rotating rocks of general, non-spherical shape. The simulated rockfall energy dissipation is validated at both the single impact and multi-impact levels using induced 780-kg rockfall experiments performed at Chant Sura, Switzerland, in 2018. Overall, the numerical results are in good quantitative agreement with the experimental measurements. Ongoing improvements of the scar drag model are to integrate rotational drag into the rock energy dissipation term, and to calibrate the drag parameters in depths using repetitive rockfall experiments spanning a greater range of rock shapes and masses.

Keywords Rockfall · Scarring drag · Non-smooth mechanics · Computational modelling · Simulation

Introduction

Rockfall is an ever-present natural hazard encountered in mountainous regions throughout the world. During the past decade, much effort has been invested to computationally model rockfall motion in order to plan measures that prevent the loss of human lives and destruction of public infrastructure (Volkwein et al. 2011; Bourrier et al. 2012; Lambert et al. 2013; Thoeni et al. 2014; Macciotta et al. 2015; Corona et al. 2017; Effeindzourou et al. 2017; Gao and Meguid 2018; Toe et al. 2018; Volkwein et al. 2018). One of the major applications of rockfall trajectory modelling is to produce hazard maps that delineate dangerous rockfall runout zones.

At first glance, rockfall modelling must appear trivial, because simple collisional mechanics can be applied to describe the rock-ground interaction. Much research has been performed that attempts to capture the energy loss of rock upon impact with terrain surface within the framework of the so-called restitution coefficient (Asteriou and Tsiambaos 2018; Gratchev and Saeidi 2018; Wang et al. 2018). The restitution coefficient can be in general defined as the ratio between the rebound and the incident velocity of rock at the impact point in both the contact normal and tangential directions (Asteriou et al. 2012). Some variations of definition exist that aim to incorporate the change of rotational motion of rock due to its collision at boundaries, such as

multiplying a weight factor to the traditional normal and tangential restitution coefficients, or utilizing instead the square root of the ratio between the rebound and the incident kinetic energy (Zhang et al. 2018). From the practical point of view, the rockfall modes incorporating restitution coefficient supply as a simplified yet powerful tool for engineers who need to derive practical and sometimes conservative risk assessment for rockfall runout zones and protection measures (Dorren 2016).

Recent real-scale field experiments in different slope conditions with rocks of natural shape, however, reveal the complexity of the rock-ground interaction (Caviezel and Gerber 2018; Caviezel et al. 2019). Falling rocks exhibit a wide range of dynamic interaction modes with the ground including *bouncing*, *rolling* and *sliding* (Li and Lan 2015). In the end, the application of restitution coefficients exhibits some limitations because it models only one particular interaction mode: bouncing. In reality, the accurate modelling of the energy dissipation during the rock-ground interaction is an extremely challenging task. The most significant problem is that rock impacts generate severe plastic deformation of the ground surface, leaving scars of varying dimensions depending on the collisional energy of rock (Gischig et al. 2015). The soil can be sheared, splashed and/or compacted in dependence of the rock's impact angle, translational velocity, rotational speed, rock mass and shape, see Fig. 1

Numerical methods that utilise restitution coefficients have at least two natural drawbacks. Firstly, they do not reflect the complexity of the rock-ground scarring phenomena such that in principle, it is only applicable to model how a small rock collides with a hard bedrock slope where negligible ground deformation is expected. One admits that this is a very rare case in practical applications. Secondly, it is extremely laborious, if not impossible, to identify a suitable restitution coefficient to reproduce the energy loss of rock at every plastic rock-ground impact. This is due to the fact that an accurate determination of a restitution coefficient relies on separating the influence of all the different factors involved in the collisional impact such as soil properties and rock geometry, size and orientation at contact. Because the restitution coefficient is mainly investigated at the single impact scale, the extension to a complete trajectory, involving multiple impacts, is difficult because of the spatial variability of the slope properties from the release to runout zone. Consequently, these models try to overcome these inherent drawbacks by incorporating Monte-Carlo stochastic processes at every impact.

The complex rock-soil interaction sets up a challenge to rigid-body rockfall models. Without incorporating rock-ground scarring, a clear picture of the rock-substrate interaction cannot be obtained. Hence, the goal of this study is to propose an energy dissipation model that incorporates rock-ground scarring effects. The new modelling scheme falls into our previously proposed non-smooth mechanics framework (Christen et al. 2012; Leine et al. 2014; Bartelt et al. 2016; Lu et al. 2018) and is applied to



Fig. 1 Chant Sura, Switzerland, 2018: Typical scars left on the terrain surface by an about 800-kg man-made rock during an induced rockfall experiment. Note the different shapes of the scars. See also the model validation part for the detailed scar dimensions

simulate three-dimensional solid rigid bodies impacting soft compactable soils. In addition, the implemented numerical method is fully applicable to generally shaped rocks undergoing rotations. The fragmentation of rock following strong impacts is not considered here since this is another challenging issue (Gang et al. 2018; Li et al. 2018), which goes beyond the scope of this study. Due to the limited rock energy investigated (kinetic energies $\ll 80$ GJ), other energy dissipation forms such as seismic wave propagation and sound dissipation coming along with extremely energetic rockfalls (Blasio et al. 2018) are likewise not of interest.

In the following sections, the theoretical aspects supporting our simulations are firstly explained in particular addressing rockfall energy dissipation due to scarring. Then, the computational mechanics algorithms are validated by using induced rockfall experimental data (Caviezel et al. 2019) obtained with in situ measurement techniques (Caviezel et al. 2018a; Caviezel et al. 2018b) at Chant Sura, Switzerland, in 2018. Note that the presented work does not aim for a detailed calibration of the governing parameters for rockfall energy dissipation; it is to demonstrate that the proposed algorithm is able to capture the essential features of a rock-ground interaction with scarring. Finally, the performance of the simulations is discussed from perspectives of both result accuracy and model feasibility.

Modelling rockfall energy dissipation incorporating rock-ground scarring

Rockfall dynamics described in non-smooth mechanics framework

To model rockfall trajectories in general, three-dimensional terrain, we apply non-smooth mechanics coupled with hard contact laws (Leine et al. 2014; Lu et al. 2018). The non-smooth approach requires two coordinate systems to model non-spherical (polyhedral) rockfalls on a three-dimensional terrain. The first one is the global, inertial-frame I , which is anchored at the origin O of the simulated system, usually given by coordinate system of the digital elevation model. The axes e_x^I and e_y^I span the horizontal plane, while the axis e_z^I extends along the vertical, counter-gravitational direction. The second one is the local, eigenframe K , which is attached to the centre of mass S of the rock. The three axes e_x^K , e_y^K and e_z^K are overlapping with the rock's principal axes of

moment of inertia. At any time t , the position and orientation of a rock are given by the generalised coordinates q :

$$q = \begin{pmatrix} r_{OS}^I \\ p_{IK} \end{pmatrix} \in \mathfrak{R}^7 \quad (1)$$

where r_{OS}^I is the positional vector connecting O and S , and p_{IK} is the four-dimensional orientation indicator, i.e. quaternion, satisfying $\|p_{IK}\| = 1$ (Lu et al. 2015). The time derivative of q leads to the dimension-reduced, generalised rock velocities u :

$$u = \frac{\partial}{\partial t} q = \begin{pmatrix} \dot{r}_{OS}^I \\ \dot{p}_{IK} \end{pmatrix} = \begin{pmatrix} V_S^I \\ \Omega^K \end{pmatrix} \in \mathfrak{R}^6 \quad (2)$$

where V_S^I is the translational velocity vector expressed in I , and Ω^K is the rotational velocity vector represented in K . The time evolution of V_S^I reads as follows:

$$\frac{\partial}{\partial t} (M_\Gamma V_S^I) = M_\Gamma \dot{V}_S^I = F_g^I + F_d^I \quad (3)$$

where M_Γ is the mass of rock. F_g^I and F_d^I are, respectively, the gravitational force and the external damping force exerting at S . The external damping force refers to the scarring drag force introduced later in the text. The air resistance is not considered (Blasio et al. 2018). Accordingly, the time evolution of Ω^K obeys Euler's equation:

$$\theta_S^K \dot{\Omega}^K + \Omega^K \times \theta_S^K \Omega^K = T^K \quad (4)$$

where θ_S^K defines the inertia tensor for the rock in K , and T^K is the additional torque generated by contact forces acting on the boundary of rock. When there is no rock-ground collision, T^K is simply set to zero. Hence, the equation of rock motion can be summarised as follows:

$$\begin{cases} M\dot{u} - h(q, u, t) = W(q)\lambda \\ M = \begin{bmatrix} M_\Gamma I_{3 \times 3} & \mathbf{0}_{3 \times 3} \\ \mathbf{0}_{3 \times 3} & \theta_S^K \end{bmatrix} \\ h(q, u, t) = \left(F_g^I + F_d^I, -\Omega^K \times \theta_S^K \Omega^K \right)^T \end{cases} \quad (5)$$

where λ is the contact force vector applying at the rock's geometrical boundary, $W(q)$ is the so-called matrix of generalised force directions transferring all the λ elements from the rock boundary

to the force and torque at the rock centre of mass, and $h(q, u, t)$ is the term containing the external damping force and the gyroscopic force generated by the non-spherical rock rotation. Equation 5 needs to be solved iteratively using time-stepping schemes (Studer et al. 2008).

Numerically, a contact is detected when at least one boundary point (vertex) of the rock ‘penetrates’ into the surface of terrain defined by the digital elevation model (Leine et al. 2014), generating an effective overlap or a negative gap G measured along e_z^I . At every contact point, a local contact frame C is constructed within the frame I specifying the contact normal and tangential directions, such that the contact forces are decomposed onto these directions. In the contact normal direction, the Signorini condition correlates the normal contact force λ_N and the gap function G following:

$$0 \leq \lambda_N \perp G \geq 0 \quad (6)$$

This formula indicates $\lambda_N \geq 0$ for a closed contact characterised by $G = 0$ (actually $G \leq 0$ is allowed in the modelling only for the contact detection purpose), and $\lambda_N = 0$ for a case of no contact with $G > 0$. In the contact tangential directions, the spatial Coulomb’s friction law is applied:

$$-V_T = \begin{cases} \{0\} & \text{if } \|\lambda_T\| < \|\mu_\Lambda \lambda_N\|, \quad \text{sticking} \\ \mathcal{R}_{\geq 0} \lambda_T & \text{if } \|\lambda_T\| = \|\mu_\Lambda \lambda_N\|, \quad \text{slipping} \end{cases} \quad (7)$$

where μ_Λ is the sliding friction coefficient. Note the mechanical structure switches from the sticking to the slipping mode if the frictional force λ_T increases and reaches the sliding frictional force $\mu_\Lambda \lambda_N$. The negative sign in Eq. 7 means that λ_T always acts along the counter-direction of the tangential velocity V_T .

Rockfall energy dissipation due to rock-ground scarring

To simulate rock-ground interaction, the terrain is divided into a plastic, deformable scarring layer Σ and a non-deformable, hard contact ‘slippage’ plane Λ . Both the scarring layer Σ and the rebound plane Λ are located below the digital elevation model. This division is the core assumption of the model. Three sub-processes are considered as follows: (1) the rock Γ enters the scarring layer Σ (scarring phase); (2) the rock Γ slides along the rebound plane Λ (sliding phase); (3) the rock Γ rebounds (rebounding phase). Table 1 defines the parameters that are used to describe a rock-ground interaction process.

To find the appropriate form of the drag resistance, we apply the work energy theorem to the collisional system consisting of the rock Γ and the scarring layer Σ , see Fig. 2. Consider first the case of a rock’s vertical drop onto a horizontal ground forming an entirely plastic collision, where the rock does not rebound out of the soil substrate and all the kinetic energy is dissipated. To simplify our derivation, we assume that the work that gravity does to the rock along the braking distance d_Σ is much smaller than that of the braking force F_d^I and thus can be omitted. In this case, the change in rock kinetic energy ΔK_Γ is proportional to the product of F_d^I and d_Σ :

$$\begin{aligned} \Delta K_\Gamma &= \frac{1}{2} M_\Gamma V_\Gamma^2 - 0 = (F_d^I - F_g^I) d_\Sigma \approx F_d^I d_\Sigma \\ &= \int_0^t F_d^I(t) \|\dot{\zeta}_\Gamma(t)\| dt \end{aligned} \quad (8)$$

where V_Γ corresponds to the speed of rock right before it contacts with the ground surface. Here, we also assume that F_d^I acts along the vertical direction; thus, d_Σ is equivalent to the maximum rock

Table 1 Parameter definitions for describing a rock-ground interaction process

Symbol	Unit	Definition
Γ		Rock
Σ		Scarring layer
Λ		Rebound plane
X, Y, Z	m	Terrain (global) coordinates
x, y, z	m	Rock (local) coordinates
t	s	Time
		Rock Γ
M_Γ	kg	Mass of rock
V_Γ	m s^{-1}	Velocity of rock
V_Γ^\perp	m s^{-1}	Vertical velocity of rock
V_Γ^-	m s^{-1}	Velocity of rock before scarring
V_Γ^+	m s^{-1}	Velocity of rock after scarring
$V_{\Gamma \rightarrow \Sigma}$	m s^{-1}	Velocity of rock during scarring
$V_{\Gamma \rightarrow \Lambda}$	m s^{-1}	Velocity of rock during sliding
$\zeta_\Gamma(t)$	m	Rock penetration depth at t
$A_\Gamma(t)$	m^2	Effective area of rock in scar at t
		Scarring layer Σ
M_Σ^e	kN m^{-2}	Soil mechanical strength
ρ_Σ	kg m^{-3}	Soil density
d_Σ^{\max}	m	Maximum rock penetration depth
l_Σ	m	Scar length on terrain surface
C_d^I		Scar drag coefficient
C_f^I		Scar drag coefficient (fluid part)
C_s^I		Scar drag coefficient (solid part)
		Rebound plane Λ
s_Λ	m	Sliding distance on rebound plane
μ_Λ		Sliding friction coefficient
μ_Λ^{\min}		Minimum friction coefficient
μ_Λ^{\max}		Maximum friction coefficient
κ_Λ		Slippage hardening coefficient
β_Λ		Slippage softening coefficient

penetration depth d_Σ^{\max} . We now express the drag force in the soil substrate as a velocity squared resistance parameterised by the scarring coefficient C_d^I , which is equivalent in form to drag defined in fluid dynamics:

$$F_d^I(t) = \frac{1}{2} C_d^I \rho_\Sigma A_\Gamma(t) \|\dot{\zeta}_\Gamma(t)\|^2 \quad (9)$$

where $A_\Gamma(t)$ is the cross-sectional area of the penetration scar. From the work energy theorem, the physical meaning of the dimensionless scarring coefficient can then be discerned,

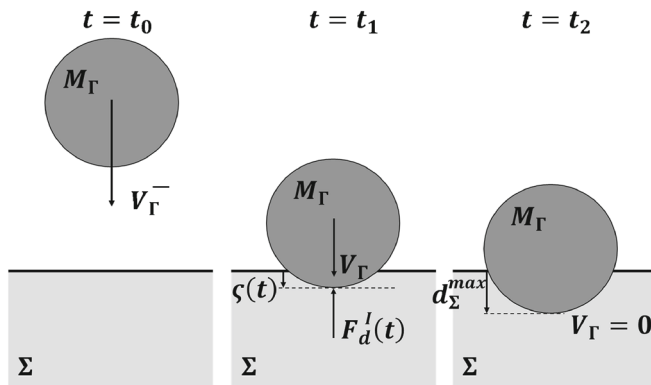


Fig. 2 To find the scarring drag parameters, we apply the work energy theorem stating that the product of the braking force F_d^I and braking distance d_Σ is equal to the loss of rock kinetic energy. The rock is simplified as a sphere

$$C_d^I \approx \frac{\frac{1}{2} \rho_\Gamma d_\Gamma^3 V_\Gamma^2}{\frac{1}{2} \rho_\Sigma \int_0^t A_\Gamma(t) \|\dot{\zeta}(t)\|^3 dt} = \frac{\rho_\Gamma d_\Gamma^3 V_\Gamma^2}{\rho_\Sigma \int_0^t \left(A_\Gamma(t) \|\dot{\zeta}(t)\| \right) \left(\|\dot{\zeta}(t)\|^2 \right) dt} \quad (10)$$

where d_Γ is a length scale of the rock, and the term $A_\Gamma(t) \|\dot{\zeta}(t)\|$ represents the incremental dimensions of the scar at time t . The significant conclusion from this analysis is that (1) the drag force acting on the rock will be parameterised as a velocity squared dependent drag, (2) the drag coefficient physically represents the ratio between the characteristic volumes of the rock and the scar and (3) the soil compacting rate can influence the drag coefficient. At least C_d^I can be approximated from field observations where maximum penetration depth d_Σ^{max} and scar length l_Σ can be measured and compared with the characteristic length of the rock d_Γ .

In the above analysis, all the kinetic energy of the rock is dissipated and the rock comes to a standstill. There is no rebound. The drag coefficient therefore provides the mean drag force over the braking distance. In reality, the soil in the scar is being compacted (or removed by splashing) and at a certain stage, the substrate can no longer deform. That is, there exists a penetration depth, denoted as d_Σ^{max} , at which the increment in braking distance becomes infinitely small. This stage marks the end of the scarring phase and the beginning of the rebound process. It can well be that this stage is reached before all the kinetic energy in the rock is lost. We thus define a mean scarring drag over the distance before the rock completely rebounds out of or stops in the scar. To simplify our calculation, it is presumed that the drag force acts at the mass centre of rock, i.e. in the scarring layer, the rock holds its moving direction and rotational speed before it reaches the rebound plane Λ where no further penetration is allowed. We now dissect the three phases of a scarring impact.

Phase 1: Scarring phase—the rock Γ enters the scarring layer Σ

Figure 3 illustrates the process that a rock Γ enters the scarring layer Σ . Right before the rock Γ enters the scarring layer Σ , the maximum scar depth (rebound depth) d_Σ^{max} that can be generated

by this impact is evaluated. Importantly, d_Σ^{max} relies not only on the mechanical strength M_Σ^e of the ground material but also on the mass, collisional speed, and even the orientation of the non-spherical rock at impact. To this end, Gerber (2019) proposed a rock penetration equation obtained through fitting the experimental data for freely, vertically dropped rocks of various masses and initial heights, and considering Hertz theory for the contact forces calculation. This formula reads as follows:

$$d_\Sigma^{max} = 0.1 \cdot M_\Gamma^{\frac{1}{3}} \cdot M_\Sigma^{e-0.4} \cdot \|V_\Gamma^\perp\|^{0.8} \quad (11)$$

where again, as listed in Table 1, d_Σ^{max} is the maximum rock penetration depth (rebound depth), M_Γ is the mass of rock, M_Σ^e is the mechanical strength of soil and V_Γ^\perp is the vertical component of rock velocity right before it touches ground surface. In this study, Eq. 11 is implemented to determine d_Σ^{max} , and the influence of terrain slope at the impact point on d_Σ^{max} is not taken into account. Note that in Eq. 11, the parameter M_Σ^e has a unit kN m^{-2} (Table 1) though the following M_Σ^e values are listed in a unit MN m^{-2} only for the purpose of simple expression.

When the rock comes into contact on the top of terrain surface, the soil layer, suffering from the external pressure, ‘flows’ around the rock-ground intersecting faces. This flow of the surrounding fine particles, alike fluid, exerts a drag force against the rock motion (Blasio et al. 2018). On the other hand, upon rock collision, the ground can be compacted. This compaction process normally leads to an increase in drag force, i.e. the drag coefficient grows as a result of particle jamming (Albert et al. 2001).

We therefore divide the scarring drag coefficient into two processes shown by:

$$C_d^I = C_f^I + C_s^I \quad (12)$$

where C_f^I is the drag coefficient accounting for the fluid behaviour of soil, and C_s^I is the additional drag coefficient taking into account of the soil compaction. Here, C_f^I is assumed to be a constant value 1.0, and C_s^I varies with soil mechanical strength M_Σ^e and rock mass M_Γ . On one hand, for a given M_Σ^e value, we anticipate a higher C_s^I for a larger M_Γ , which in general corresponds to a deeper penetration depth d_Σ^{max} . On the other hand, for a given M_Γ value, one expects that C_s^I decreases with decreasing M_Σ^e as it is more difficult to build up a high resultant stress and thus a strong local plastic yielding in a looser granular media.

Phase 2: Sliding phase—the rock Γ slides along the rebound plane Λ

Figure 4 shows the second phase for the rock-soil interaction that a rock Γ slides along the rebound plane Λ . Λ is formed when the rock cannot compress the soil any further; thus, it is equivalent to a hard, non-deformable ground. At this stage, in the scarring layer, the rock can no longer move along the ground normal direction but slide forwards on Λ . In addition to the scarring drag force, the rock is subjected to a frictional force changing over time, resulting in a rock velocity $V_{\Gamma \rightarrow \Lambda}$ and a subsequent change of the moving direction and the rotational velocity. Slippage along the hard, non-deformable contact plane is governed by the Coulomb’s friction law, i.e. $\lambda_T = (s_\Lambda) \lambda_N$, where the frictional force λ_T is non-linearly correlated with the normal contact force λ_N due to the fact that material accumulation with slippage distance s_Λ causes the

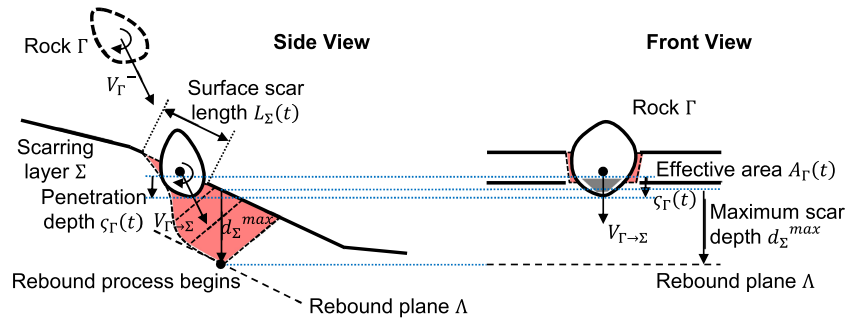


Fig. 3 Scarring phase: the rock Γ enters the scarring layer Σ . The rock is penetrating a vertical distance $\zeta_{\Gamma}(t)$ until it reaches the rebound plane Λ . The velocity of the rock at this stage is $V_{\Gamma \rightarrow \Sigma}$. The sliding phase begins when the penetration depth is equal to the maximum scar depth $\zeta_{\Gamma}(t) = d_{\Sigma}^{\max}$. The scarring drag force experienced by the rock in the scarring layer is proportional to its frontal, effective area $A_{\Gamma}(t)$, i.e. the projected area of the rock-soil intersecting body onto a plane that is perpendicular to the rock velocity. Note that $A_{\Gamma}(t)$ depends on rock orientation, velocity direction and penetration distance

frictional coefficient μ_{Λ} to increase (Leine et al. 2014). This process is described using the following equation:

$$\mu_{\Lambda}(s_{\Lambda}) = \mu_{\Lambda}^{\min} + \frac{2}{\pi} \cdot (\mu_{\Lambda}^{\max} - \mu_{\Lambda}^{\min}) \cdot \arctan(\kappa_{\Lambda} s_{\Lambda}) \quad (13)$$

κ_{Λ} controls how fast the increase in μ_{Λ} will force the rock to jump away from Λ . Equation 13 raises $\mu_{\Lambda}(s_{\Lambda})$ as long as one active contact point is detected between the rock and the rebound plane; otherwise, s_{Λ} decays according to a factor β_{Λ} following Eq. 14, which, in turn, decreases $\mu_{\Lambda}(s_{\Lambda})$ with time obeying Eq. 13 until μ_{Λ}^{\min} is reached:

$$\dot{s}_{\Lambda} = -\beta_{\Lambda} s_{\Lambda} \quad (14)$$

Phase 3: Rebounding phase—the rock Γ rebounds

Figure 5 shows the last phase for the rock-soil interaction: the sliding phase ends when the contact of rock with the rebound plane breaks. This rebounding phase continues until the rock completely leaves the scarring layer Σ . Again, it is assumed that during this process, the rock does not change its moving direction and rotational speed but still experiences scarring drag force. After completion of rock-ground interaction, the rock travels at V_{Γ}^{+} . In general, $V_{\Gamma}^{+} < V_{\Gamma}^{-}$ due to energy dissipation, but $V_{\Gamma}^{+} > V_{\Gamma}^{-}$ is possible for highly elastic impacts (Caviezel et al. 2019).

Meanwhile, a final scar length l_{Σ} can be observed on the surface of terrain showing the effective range of this impact.

Validation of the rockfall energy dissipation model using induced rockfall experiments

In this section, we validate the proposed scarring model by comparing simulation results with energy dissipation data acquired from induced rockfall experiments. We use both single ground impact and entire trajectories that is multi-ground impacts. The aim of the work is to scrutinise how Eq. 9 (scarring drag) and Eq. 11 (penetration distance to rebound) behave and thus to validate whether the energy dissipation due to rock-ground impacts can be precisely simulated using this modelling approach.

Setup of rockfall experiments at Chant Sura in Switzerland

The setup for the full-scale, induced rockfall experiments is presented in detail by Caviezel et al. (Caviezel et al. 2019) and will not be entirely repeated here except to mention the key experimental conditions. The experiments were performed at Chant Sura (Fig. 6, slope angles, 40–80°, WGS 84: 46.74625, 9.96720), which is approximately 12 km south-east of Davos, Switzerland. The release platform (the inset of Fig. 6) was installed at an altitude of 2380 m above sea level. The path of a falling rock can be sequenced into three parts: (1) the acceleration zone, i.e. the region from the releasing point to the upper side of the almost vertical cliff, (2)

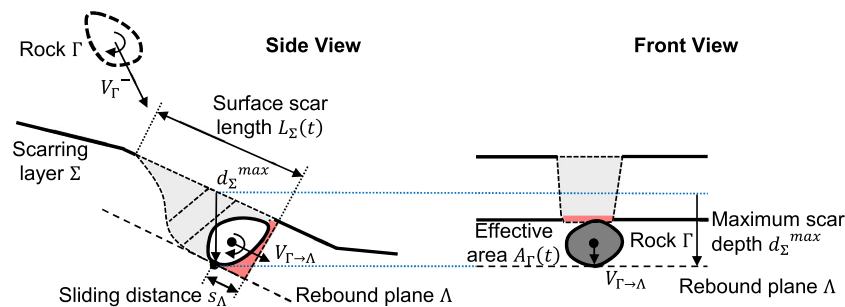


Fig. 4 Sliding phase: the rock Γ slides along the rebound plane Λ . This process begins when the penetration depth is equal to the maximum scar depth $\zeta_{\Gamma}(t) = d_{\Sigma}^{\max}$. The frictional coefficient increases while rock slips on the rebound plane Λ . The velocity of the rock at this stage is $V_{\Gamma \rightarrow \Lambda}$. The sliding phase ends when the contact of rock with the rebound plane is broken

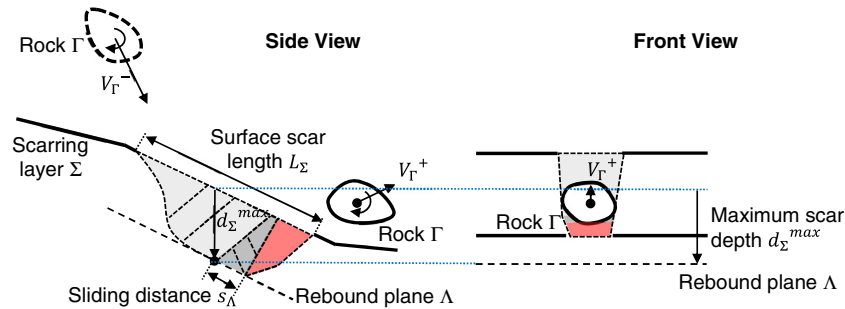


Fig. 5 Rebounding phase: the rock Γ rebounds. Scarring drag still acts on the rock during the rebounding phase, which ends when the rock completely detaches from the scarring layer Σ

the transition zone, i.e. the region between the lower side of the cliff and the beginning of the scree field and (3) the deposition zone, i.e. the scree field. In Fig. 6, the upper and lower boundaries of the cliff and the beginning of the scree field are marked using red, dotted lines. The yellow, dashed line indicates the general rock propagation on the terrain surface, which was observed in the experiments and is used later for the single impact validation. Note three-dimensional trajectory reconstruction methods are addressed in detail by Caviezel et al. (Caviezel et al. 2019).

A 780-kg man-made, perfectly symmetric, platy rock (dimensions on the major axes of moment of inertia: $0.93 \times 0.93 \times 0.47$ m), a standardised boulder shape regulated by the official European Technical Assessment Approval Guidelines, was used in the experiments. The in situ sensor, mounted as accurately as possible at the rock centre of mass, measured translational accelerations along (e_x^I, e_y^I, e_z^I) up to 400 g and rotational velocities around (e_x^K, e_y^K, e_z^K) up to $4000^\circ \text{ s}^{-1}$ with a recording frequency of 1000 Hz. In order to precisely reconstruct the rockfall trajectory, the surface resolution of the digital elevation model was originally

gained at a 5-cm scale and the altitude uncertainties were ± 3 cm. The rock translational velocities during the airborne phase, between any two neighbouring scars, were retrieved via high-resolution stereoscopic videogrammetry (Caviezel et al. 2019). The rock rotational velocities, during the whole falling process, were directly read out from the gyroscopic sensor. The scar dimensions were manually measured in the field, with the scar length l_Σ being the maximum size of scar on the slope surface measured along the rock moving direction, and the scar depth d_Σ^{max} being the vertical distance from the deepest point in the scar to the slope surface.

Setup of numerical environment for rockfall simulations

The numerical environment for our rockfall simulations is established as follows. The rock of the same shape and mass is constructed by using a polyhedron with 24 vertices. The resolution of the digital elevation model is set to 0.5 m, which is comparable with the smallest dimension of the rock. In order to start a rock single impact simulation to compare with the experimental data,

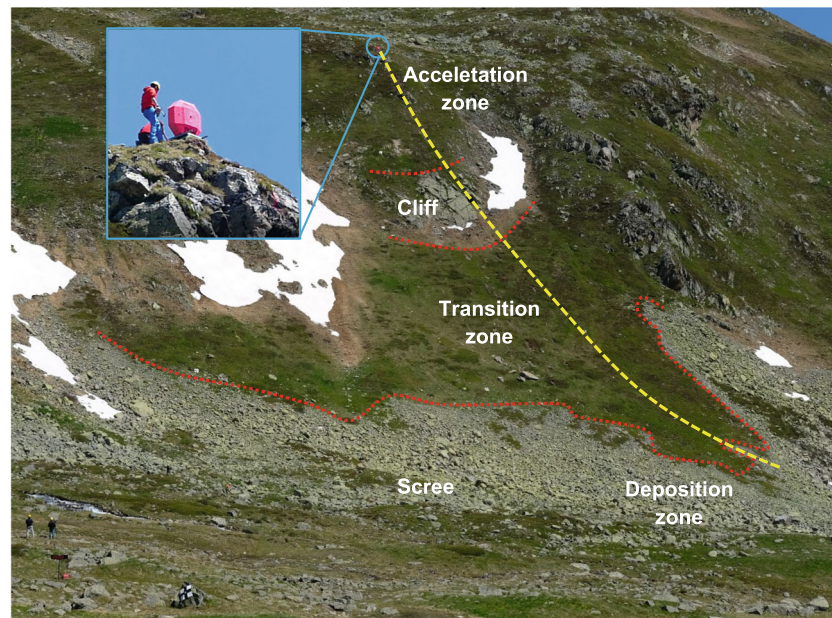


Fig. 6 Rockfall testing environment at Chant Sura, Switzerland, in 2018. A 780-kg man-made platy rock was transported by helicopter to a plateau of 2380 m high above sea level and repetitively released, resulting in a running distance of approximately 250 m on the slope. One general rock propagation path observed in the experiments is indicated using a yellow, dashed line. The terrain topography is divided into three parts: the acceleration zone that is before the cliff, the transition zone that is between the cliff and the scree and the deposition zone that is the scree. The boundaries of these regions are marked using red, dotted lines

Table 2 Key parameters reconstructed/measured from the experiments for 4 rock-ground impact dynamics

Impact	1	2	3	4
T^{start} (s)	1691.92	1692.89	1693.58	1694.32
Rock Γ				
V_{Γ}^X (m s ⁻¹)	5.56	5.30	5.34	5.34
V_{Γ}^Y (m s ⁻¹)	-14.62	-12.70	-12.31	-14.19
V_{Γ}^Z (m s ⁻¹)	-11.20	-10.74	-10.36	-8.52
V_{Γ}^{res} (m s ⁻¹)	19.24	17.46	16.95	17.39
ω_{Γ}^x (rad s ⁻¹)	-23.55	-25.98	-29.21	-28.59
ω_{Γ}^y (rad s ⁻¹)	-0.19	3.97	-2.61	-1.87
ω_{Γ}^z (rad s ⁻¹)	3.75	1.09	-0.13	-1.56
$\omega_{\Gamma}^{\text{res}}$ (rad s ⁻¹)	23.85	26.30	29.33	28.69
Scarring layer Σ				
d_{Σ}^{exp} (m)	0.13	0.15	0.18	0.21
l_{Σ}^{exp} (m)	1.40	1.80	1.55	1.52
$X_{\Sigma}^{\text{start}}$ (m)	2793293.57	2793297.18	2793300.21	2793303.71
$Y_{\Sigma}^{\text{start}}$ (m)	1180191.09	1180181.46	1180173.11	1180163.68
$Z_{\Sigma}^{\text{start}}$ (m)	2307.06	2299.46	2292.43	2286.58

one follows the following steps to specify rock dynamics (see also Table 2 for the key parameters reconstructed/measured from the experiments):

- **Starting position:** Referring to the yellow, dashed line in Fig. 6, the coordinates $X_{\Gamma}^{\text{start}}$ and $Y_{\Gamma}^{\text{start}}$ are determined using one arbitrary position on the ballistic trajectory of the rock, that is reconstructed from the experiments by Caviezel et al. (Caviezel et al. 2019), before the rock collides with terrain surface. The coordinate $Z_{\Gamma}^{\text{start}}$ is adjusted such that the virtual rock reaches the terrain surface at the same instant as in the experiment.
- **Translational velocity:** The translational velocities of the real rock extracted along (e_x^l, e_y^l, e_z^l) at the starting position are set to the virtual rock.
- **Initial orientation:** The initial orientation of the virtual rock is carefully positioned such that it is rolling downwards the slope following the actual rock moving direction.
- **Rotational velocity:** The resultant rotational speed of the real rock obtained at the starting position is applied to the virtual rock on the major axis of moment of inertia e_z^K , aligning with the rotational direction of the real rock, without taking into account the small rock wobbling around e_x^K and e_y^K .

Based on the scar measurement data that we have obtained, only the middle part of the region between the cliff and the scree (i.e. the altitude is between 2276.55 and 2310.14 m) is analysed, which includes in total 4 rock-ground impacts (Table 2). The correspondingly generated scars' dimensions are shown in Fig. 7.

The time step for the simulations is 0.002 s and rock dynamics data is output every time step. It is validated that 0.002 s is sufficiently accurate for our simulations by comparing the changes of rock energy with those obtained at an even smaller time step 0.001 s. Each simulation lasts 1 s ensuring that at the end the rock jumps out of the scar again. We assume that ρ_{Σ} is a typical, constant value of 1700 kg m⁻³ (Dorren 2016). At the rebound plane, a fixed parameter set is utilised as follows (Bartelt et al. 2016): $\mu_{\Lambda}^{\text{min}} = 0.55$, $\mu_{\Lambda}^{\text{max}} = 2.0$, $\beta_{\Lambda} = 185$ and $\kappa_{\Lambda} = 3$.

The following model validation procedures are further carried out for evaluating each single impact listed in Table 2:

- **Determining the rock incident velocity:** The vertical component V_{Γ}^{\perp} of V_{Γ}^{-} is selected from the reconstructed experimental rockfall trajectory right before the rock enters the scarring layer Σ .
- **Determining the range of soil mechanical strength:** Based on the known V_{Γ}^{\perp} and the measured scar depth d_{Σ}^{max} , a proper range of the soil mechanical strength M_{Σ}^e (± 1 MN m⁻²) can be determined.
- **Determining the scar drag coefficient:** The scar drag coefficient C_s^l is tuned in order to obtain the comparable V_{Γ}^{\perp} and l_{Σ} with the experimental data.

Finally, the averaged M_{Σ}^e and C_s^l are utilised for performing the whole trajectory simulation at Chant Sura and the results (e.g. translational and rotational velocities, jump height and jump length) obtained are compared with the 5 experimental runs (Caviezel et al. 2019) on statistical levels.

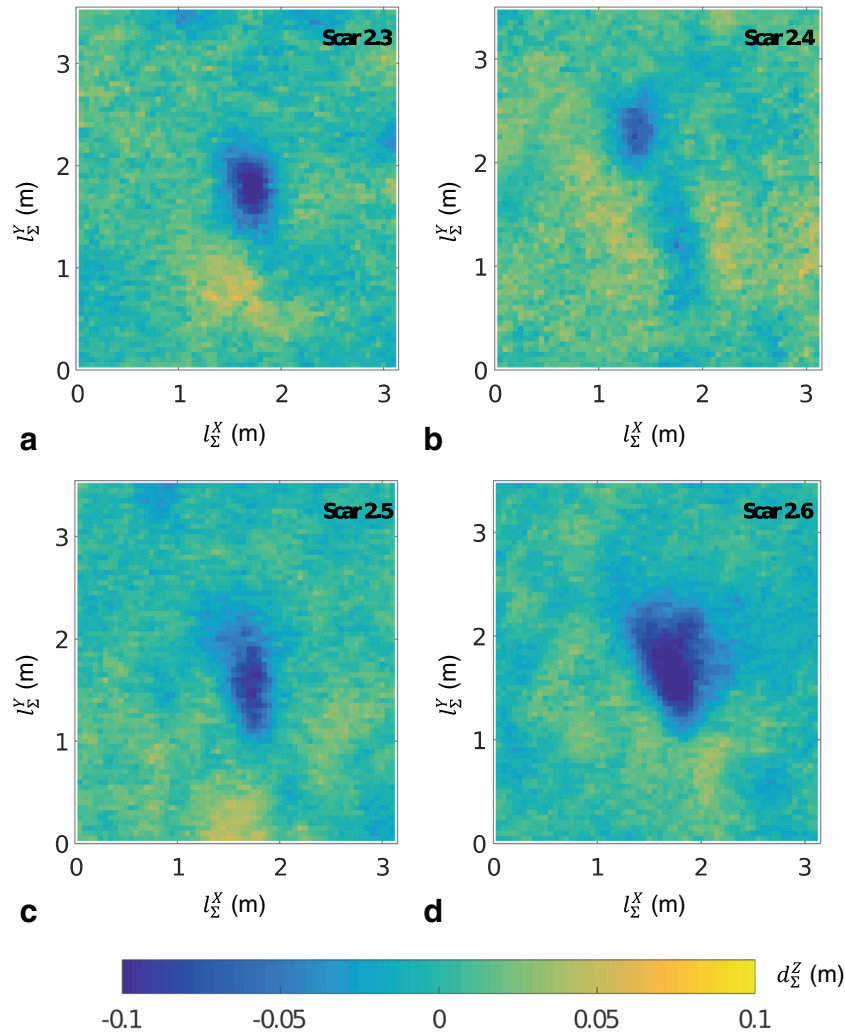


Fig. 7 The spatial dimensions of scars reconstructed from rockfall experiments corresponding to the impact (a) 1, (b) 2, (c) 3 and (d) 4 listed in Table 2, respectively

Rockfall energy dissipation on a single impact level

Figure 8 compares rockfall energy dissipation on a single impact level between the experiments and simulations. For each impact, 5 simulations are performed with varying M_{Σ}^e in a given range of $\pm 1 \text{ MN m}^{-2}$. Note that different simulations may result in the same energy change due to the small variation of M_{Σ}^e and thus the maximum scar depth, which would lead to the identical contact condition between the rock and ground for the given time step. In experiments, the rock-ground impacts last about 0.2 s, and before impact, the rock's rotational energy is approximately only 20% of its translational energy. The small modulating of the gyroscopic data steering during the rock's airborne phase is due to slight misalignment of the in situ sensor with respect to the rock's centre of mass. Interestingly, by well controlling M_{Σ}^e and C_s^I values, it is feasible to accurately reproduce the translational energy loss but only to approximately predict the rotational energy trend for the rock. This is not very surprising since our scar drag model assumes that the scarring drag force acts at the rock centre of mass, i.e. no additional torque would be exerted on the object. Depending on the rock dynamics and slope conditions, the actual impacts might even speed up the rotation (Fig. 8b and d). In simulations, this leap of rotational

speed can be only reflected by the hard contact between rock and the rebound plane such that the contact forces generate a torque which 'aligns' with the current rotational direction.

Table 3 further lists the scar depths d_{Σ}^{sim} and scar lengths l_{Σ}^{sim} obtained for the 4 impacts from simulations. One notices that these results are already in a very comparable shape with the experimental values (listed in the brackets in Table 3). In addition, (1) M_{Σ}^e varies on a slope between different impacts, depending on the composition of the granular material at the impact site; (2) C_s^I tends to be higher when M_{Σ}^e is larger, i.e. the harder soil material can exert more drag to the rock; (3) for the same M_{Σ}^e and similar d_{Σ}^{sim} , the value of C_s^I seems to be on a comparable level; nonetheless, it is difficult to clearly identify a correlation between d_{Σ}^{sim} and C_s^I as the soil compacting rate might also have an influence on C_s^I (see Eq. 10).

Rockfall energy dissipation on a complete trajectory level

For the validation of rockfall energy dissipation on a complete trajectory level, we assume that the entire slope is composed of a homogeneous soil material, i.e. $M_{\Sigma}^e = 15 \text{ MN m}^{-2}$ and $C_s^I = 1.5$. Although this assumption is very rough, it allows us to have the

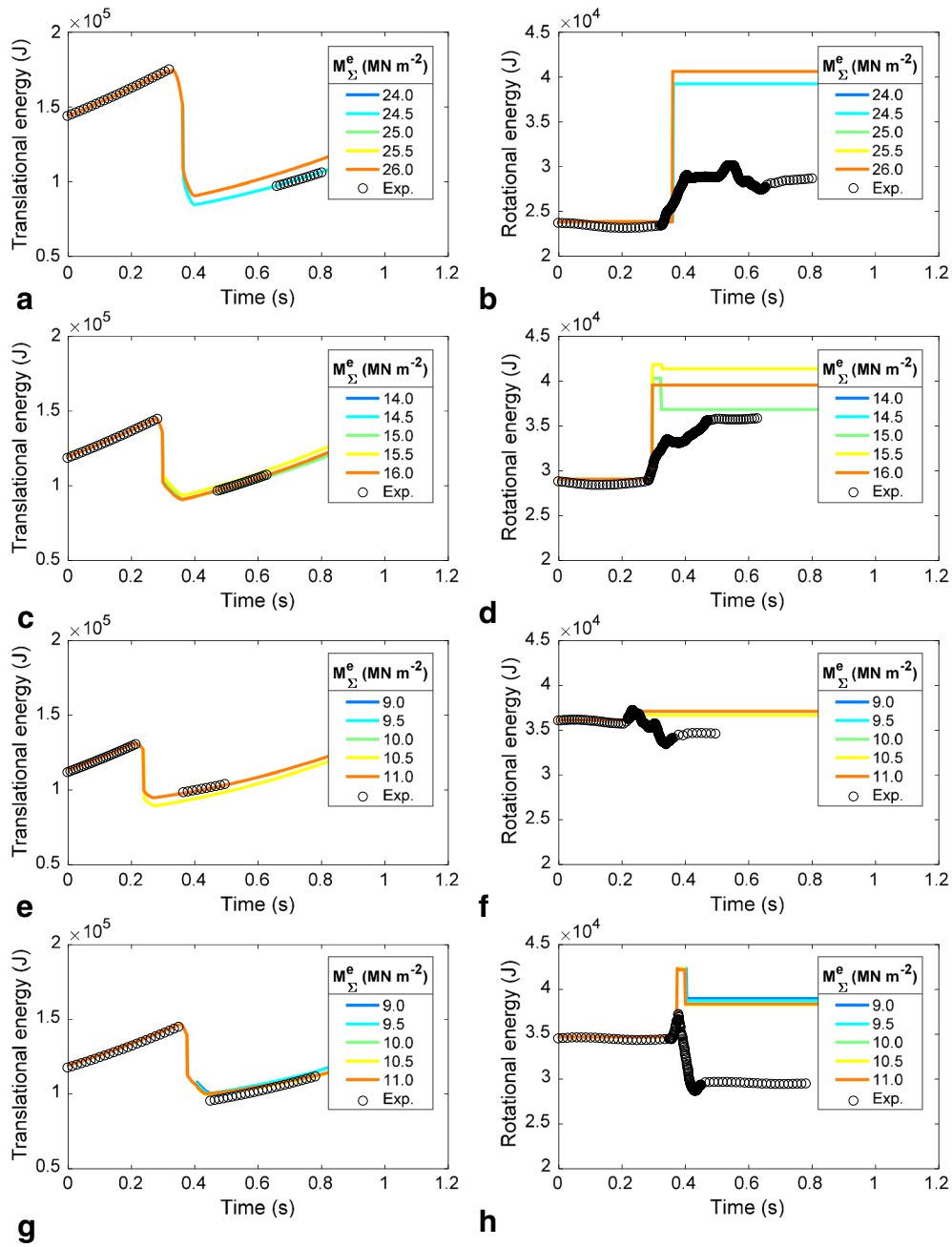


Fig. 8 Comparison of rock translational (a, c, e, g) and rotational (b, d, f, h) energy change as a function of time due to the single impacts (Table 2) obtained from experiments (black circle) and simulations (coloured lines): impact 1 (a, b); impact 2 (c, d); impact 3 (e, f); impact 4 (g, h). For each impact, 5 simulations are performed with only varying the soil mechanical strength M_{Σ}^e in a small range ($\pm 1 \text{ MN m}^{-2}$). Note the differences in the translational and rotational energy magnitudes

Table 3 Numerically obtained soil mechanical strength M_{Σ}^e , scar drag coefficient C_s^I , scar depth d_{Σ}^{sim} and scar length l_{Σ}^{sim} for the impacts listed in Table 2. The measured scar depth d_{Σ}^{exp} and scar length l_{Σ}^{exp} are again shown in the brackets for the comparison purpose

Impact	$M_{\Sigma}^e \text{ (MN m}^{-2}\text{)}$	C_s^I	$d_{\Sigma}^{sim} \text{ (} d_{\Sigma}^{exp} \text{) (m)}$	$l_{\Sigma}^{sim} \text{ (} l_{\Sigma}^{exp} \text{) (m)}$
1	25	4.0	0.14 ± 0.01 (0.13)	1.80 ± 0.02 (1.40)
2	15	1.5	0.16 ± 0.01 (0.15)	1.64 ± 0.02 (1.80)
3	10	0.1	0.18 ± 0.01 (0.18)	1.26 ± 0.01 (1.55)
4	10	0.5	0.18 ± 0.00 (0.21)	1.77 ± 0.25 (1.52)

first investigation on how the scar drag model is performing in capturing rock's energy for an entire trajectory path. The virtual rock is at start placed at the same release point as in the experiments (the rock centre of mass has a 1 m offset along e_z' relative to the terrain surface). Before releasing, the rock is given a random orientation and an initial speed -1 m s^{-1} along e_y' that is pointing to the downward slope. Originally, the rock rotational velocities are zeros. In total, 5000 independent simulations are performed.

As we concentrate on validating the scar drag model incorporating rock-soil interactions, only the slope region before the scree field is considered for analyses. Here, the acceleration zone (region 1) refers to an altitude $Z \geq 2338 \text{ m}$, and the transition zone (region 2) refers to an altitude $2267 \leq Z < 2338 \text{ m}$. As first tests, random 5 rock trajectories from the 5000 simulations are selected to compare with the data acquired from the 5 experimental runs (Caviezal et al. 2019). The box plots showing 1.5 times inter quartile range (IQR) containing about 99% of the population and the probability density functions (PDFs) are displayed for the simulations and experiments using several observed rock quantities over the entire falling process: translational speed, rotational speed, jump height and jump length. Jump height is defined as the plumb-vertical distance from the rock centre of mass S to the terrain surface, while jump length is determined as the linear distance from the projection of S on the terrain surface during rock's free flight to the one previous projection of S on the terrain surface when the rock just detaches from the scarring layer Σ . Note that all the above quantity values are collected every measuring/modelling time step, excluding, however, the time when the rock is in contact with Σ . Subsequently, as many as 500 random 5 rock trajectories are repetitively selected from the 5000 simulations for calculating the averaged rock quantity values. According to the central limit theorem, the distributions of these sample averages should obey normal distribution functions, and the means of these samples provide us good estimations for the means of the population. It is thus interesting to identify how close the numerical means are lying relative to the experimentally observed values.

Figures 9, 10, 11 and 12 plots on statistical levels, respectively, the rock translational speeds, rotational speeds, jump heights and jump lengths using a randomly selected 5-trajectory sample from the simulations. The results are also compared with those of the 5 experimental runs. It is immediately noticeable that the rock is moving faster and becoming more jumpy after the cliff (region 2) than before the cliff (region 1). Overall, one finds good agreement between the numerical and experimental results in region 1. However, in region 2, the agreement seems to be poorer. The translational and rotational speed of the virtual rock is approximately centred around 17 m s^{-1} and $1700^\circ \text{ s}^{-1}$, respectively, at the same time corresponding to a smaller maximum moving speeds compared with those of the real rock. In addition, the jump height and length of the virtual rock are larger in contrast to those of the real rock. These observations can be linked to at least two facts: (1) The scar drag model does not integrate the effect of scarring drag force on the rock rotational speed, while in reality, this force can either speed up or slow down a rock's rotation (see Fig. 10d where the range of the experimental PDF is wider than in the numerical one). This explains the exceptional performance of the model in region 1 where the translational and rotational speeds of rock are both relatively small, such that the influence of a rotational drag on rock dynamics is not

evident. (2) Owing to the method to estimate the maximum rock penetration depth (Eq. 11) and the proportion of the scarring drag force to the rock translational speed (Eq. 9), the less 'dynamic', virtual rock will tend to generate shallow scars and lose less energy during scarring, leading, in turn, to a larger jump height and length compared with the real rock.

Figure 13 further shows the virtual rock's translational speeds, rotational speeds, jump heights and jump lengths in regions 1 and 2, using data of 500 randomly selected 5-trajectory samples from the 5000 simulations. The aim of this test is to avoid the potential risk of collecting a biased 5-trajectory sample in Figs. 9, 10, 11 and 12. As expected, the distributions of these sample averages can be well fitted by normal distribution functions. In addition, almost all the mean quantity values, calculated using the 5 experimental runs, lie within the tail of the normal distribution curves, except that in region 2, the experimentally averaged jump length is significantly smaller in contrast to that of the modelling (see Fig. 13h). Moreover, Fig. 13b and d show that the virtual rock moves slower but rotates faster compared with the real one. Again, based on the current numerical algorithms, the disagreement observed above can be attributed to the facts showcased in Figs. 9, 10, 11 and 12 that (1) in our simulations, the rock rotational energy acts as an energy reservoir affecting rock translational energy and jump conditions, and (2) the less 'dynamic', virtual rock will tend to experience less scarring drag force yielding a relatively larger jump height and length in comparison with the real rock (Fig. 13f and h).

On the performance of scar drag model in rockfall energy dissipation

We are aware that there are no 'true' values for the studied rockfall dynamics, in particular considering that only 5 experimental runs are under investigation here. However, by performing one sample t test (two-tailed) over the limited experimental data, we are able to interpret from a perspective of statistical significance, the performance of the scar drag model in reproducing at least these 5 rocks' energy dissipation. Hence, we continue with one sample t test (two-tailed) with 5% significance to access if a null hypothesis is valid. The null hypothesis, or H_0 hypothesis, assumes that there exists no statistically significant difference between the 'true' mean of the experimental results and the mean of the numerical results. This analysis predicts for rock dynamic quantities, i.e. translational and rotational speeds, jump height and jump length, the probability p value of obtaining a discrepancy at least the same magnitude as the observed discrepancy shown in Fig. 13. A p value corresponding to 5% or less indicates that it is very unlikely in reality to observe the given numerical results under H_0 hypothesis. The testing results obtained are shown in Table 4. Most of the H_0 hypothesis are rejected based on the employed numerical parameters M_{Σ}^e (15 MN m^{-2}) and C_s^l (1.5), which is apparent from Fig. 13 because most of the experimentally obtained mean quantity values are close to the tail of the numerically fitted normal distribution curves. Nonetheless, it is premature to directly conclude that our simulations overall underfit the experimental data. At least more experimental data should be collected in the future to give us more valid, 'true' rock dynamic quantities for comparison purpose.

The above one sample t test also points to another issue: should one consider the practical significance when explaining the comparison results between simulations and experiments? The answer

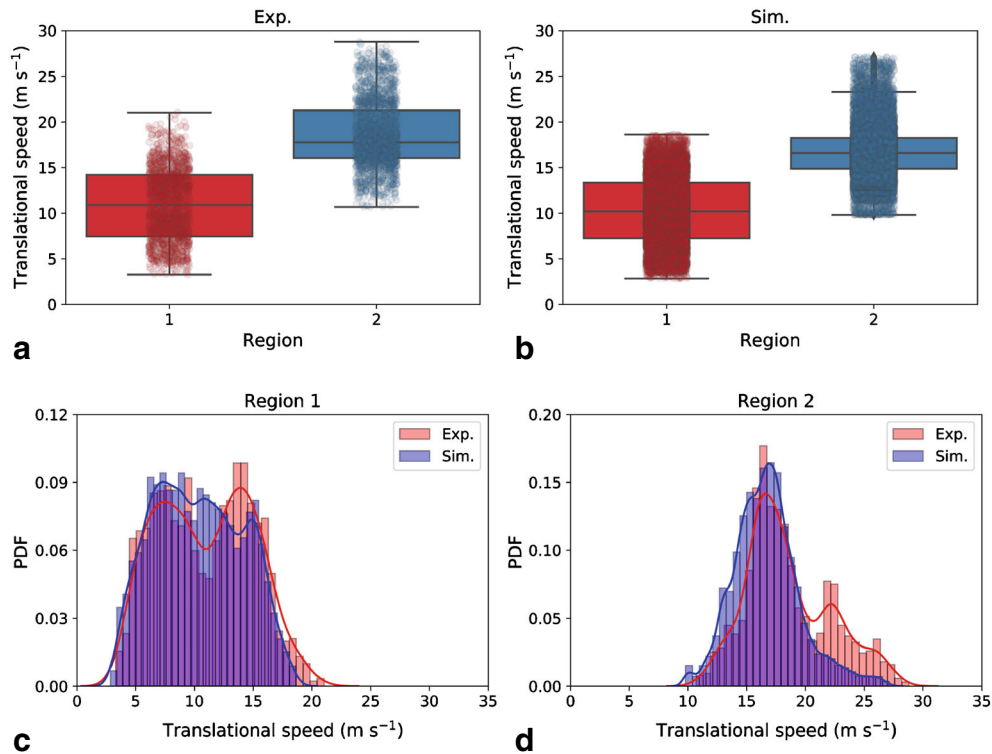


Fig. 9 Statistical plots of rock translational speeds from a randomly selected 5-trajectory sample (region 1: acceleration zone; region 2: transition zone). a, b Box plots of translational speeds in experiments (a) and simulations (b). c, d Probability density functions of translational speeds in region 1 (c) and region 2 (d)

is yes. Because it is highly likely that one achieves an observation which is statistically significant but might not be practically significant. For instance, in region 2, the rock rotates with an average

speed of $1652.72^{\circ} \text{ s}^{-1}$ in experiments and $1745.29^{\circ} \text{ s}^{-1}$ in simulations (see Fig. 13d). If $1652.72^{\circ} \text{ s}^{-1}$ were already obtained from averaging a ‘sufficiently’ large experimental data set (in practice,

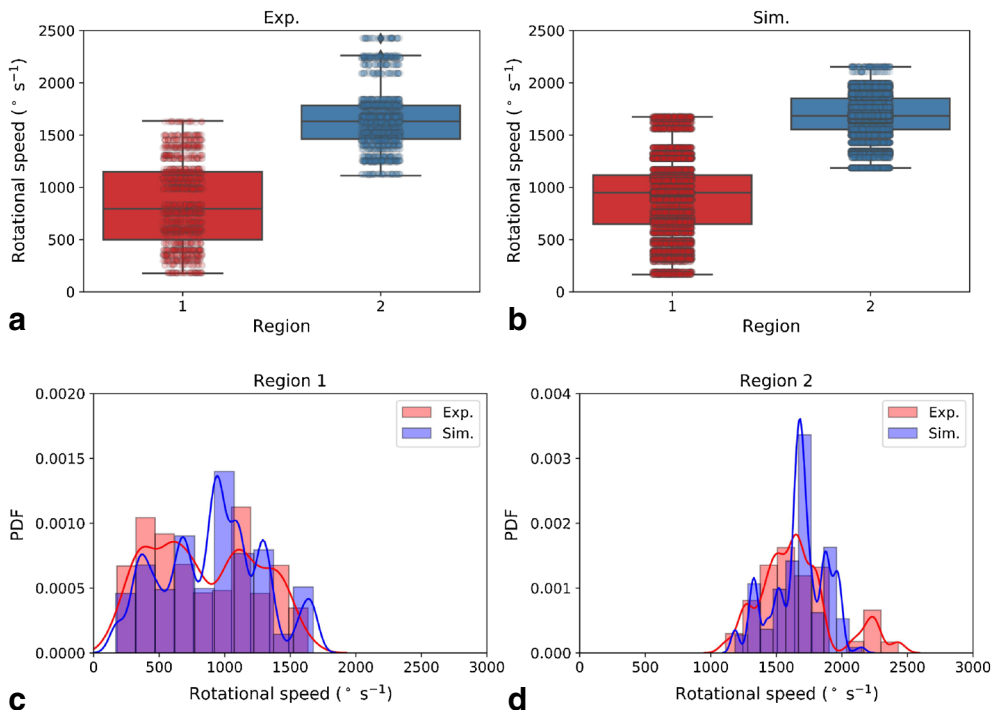


Fig. 10 Statistical plots of rock rotational speeds from a randomly selected 5-trajectory sample (region 1: acceleration zone; region 2: transition zone). a, b Box plots of rotational speeds in experiments (a) and simulations (b). c, d Probability density functions of rotational speeds in region 1 (c) and region 2 (d)

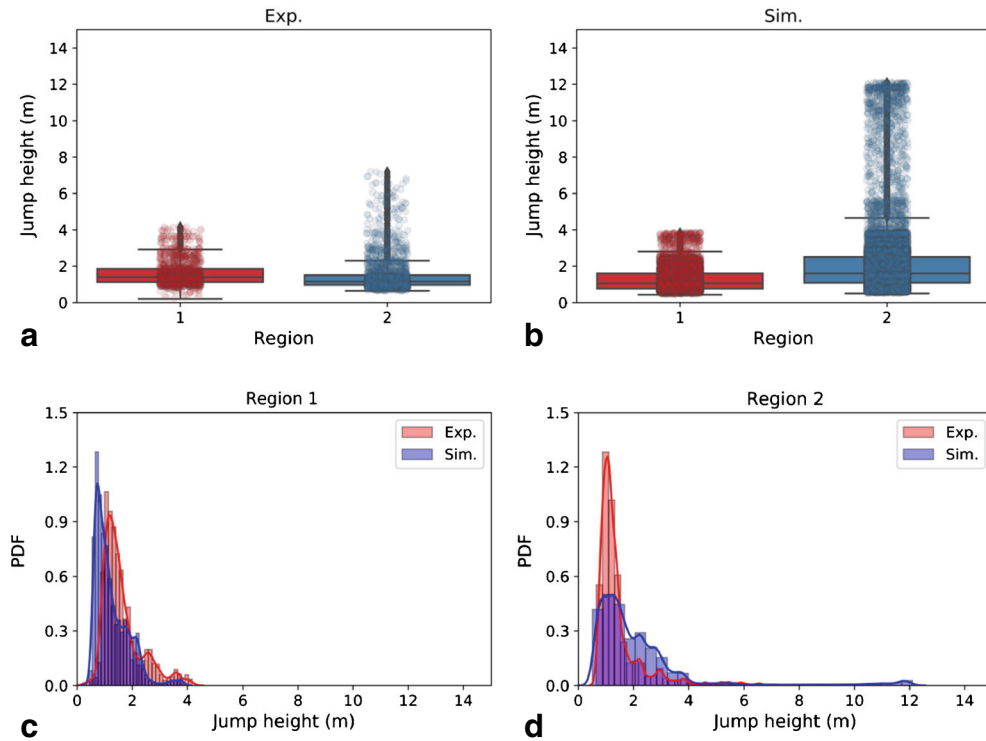


Fig. 11 Statistical plots of rock jump heights from a randomly selected 5-trajectory sample (region 1: acceleration zone; region 2: transition zone). **a, b** Box plots of jump heights in experiments (a) and simulations (b). **c, d** Probability density functions of jump heights in region 1 (c) and region 2 (d)

this is almost never possible), one would ask whether this about 5% difference relative to the experimental data in rotational speed

is of any practical interest. On the other hand, an excessively finely tuned set of numerical parameters based on the limited

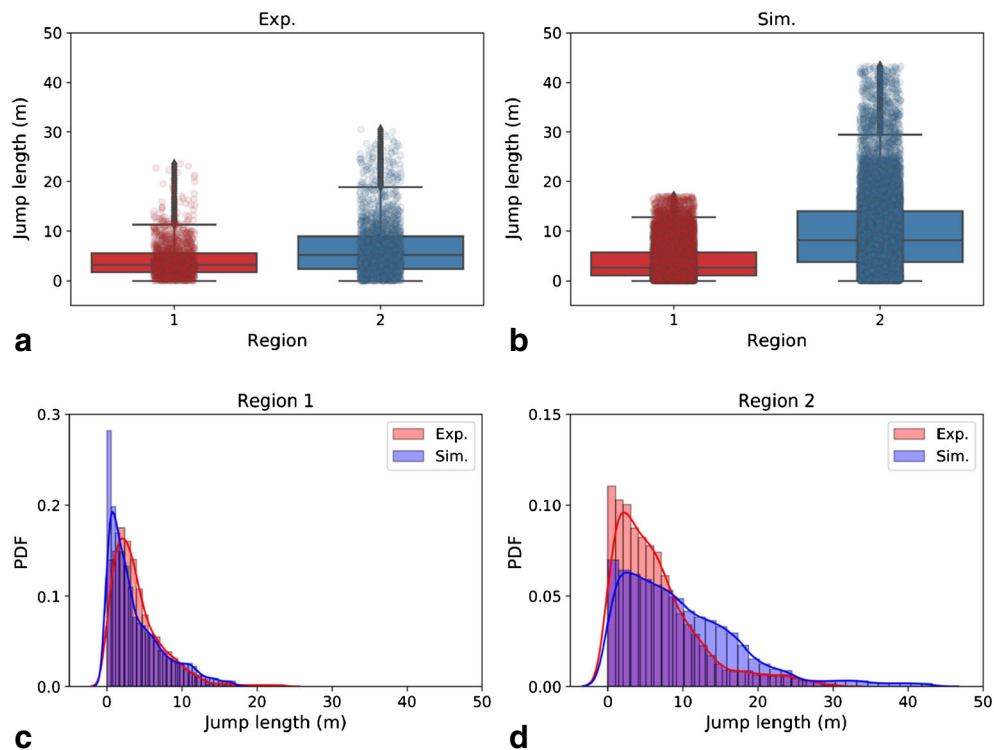


Fig. 12 Statistical plots of rock jump lengths from a randomly selected 5-trajectory sample (region 1: acceleration zone; region 2: transition zone). **a, b** Box plots of jump lengths in experiments (a) and simulations (b). **c, d** Probability density functions of jump lengths in region 1 (c) and region 2 (d)

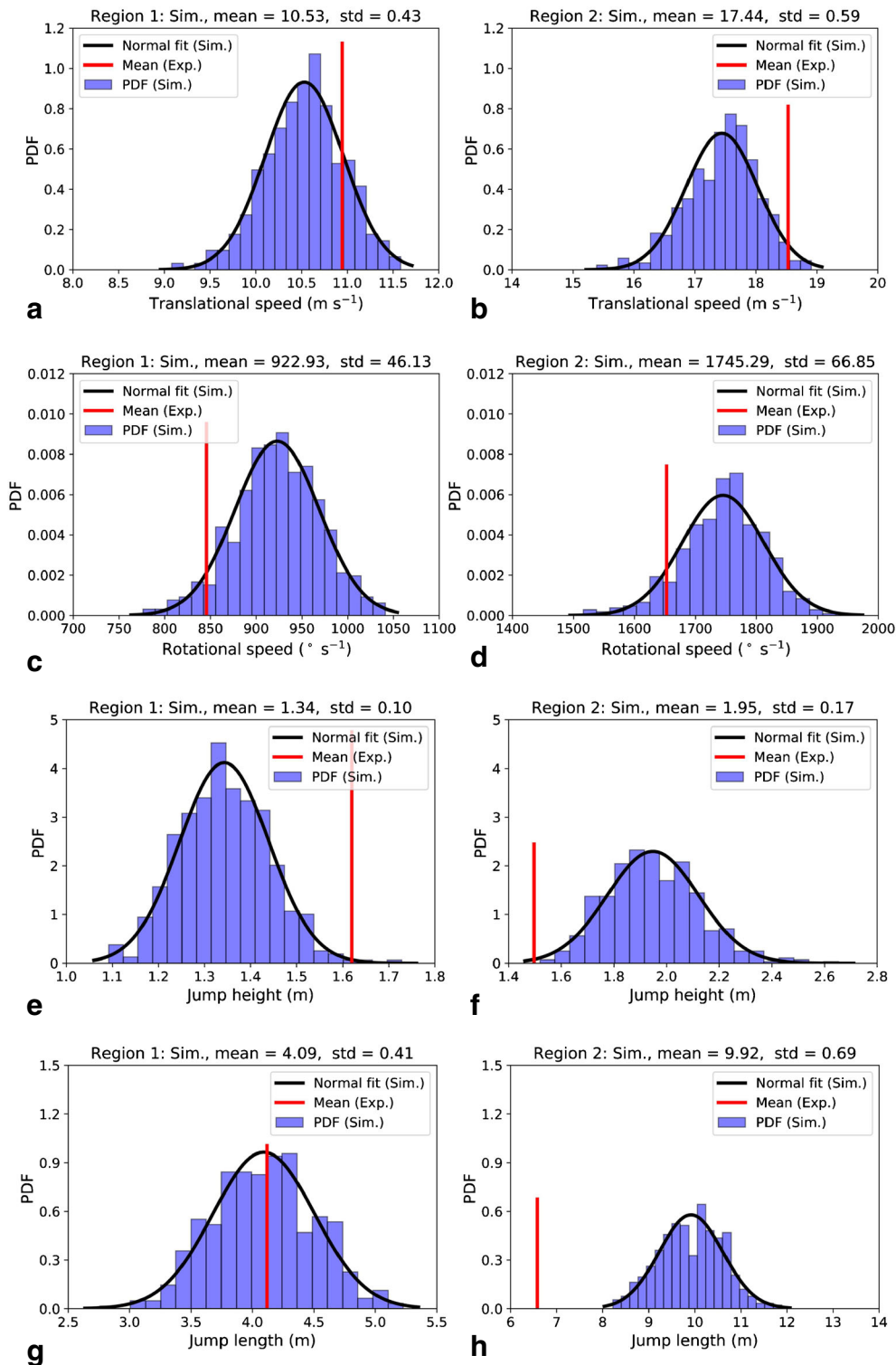


Fig. 13 Statistical plots of rock translational speed (a, b), rotational speed (c, d), jump height (e, f) and jump length (g, h) in region 1 (a, c, e, g) and region 2 (b, d, f, h) obtained from both experiments and simulations. The histograms (blue), fitted by the normal distribution functions (black), are corresponding to 500 randomly selected 5-trajectory samples from the 5000 simulations. The red, solid lines show the mean rock quantity values calculated via using the 5 experimental runs

experimental data may even cause overfitting problems to the models, which means the models can only well simulate the existing rockfall trajectories but will fail to ‘predict’ the future

rockfall dynamics. This is apparently worth paying attention to when developing rockfall simulation software only aiming for an ‘exact’ match between the modelling and existing events.

Table 4 Performing one sample t test (two-tailed) with 5% significance under H_0 hypothesis over the key rock dynamic quantities using the experimental and simulation results shown in Fig. 13

Region	Dynamic quantity	<i>p</i> value	H_0 test
1	Translational speed	<0.0001	Reject
	Rotational speed	<0.0001	Reject
	Jump height	<0.0001	Reject
	Jump length	0.1024	Accept
2	Translational speed	<0.0001	Reject
	Rotational speed	<0.0001	Reject
	Jump height	<0.0001	Reject
	Jump length	<0.0001	Reject

One advantage of the proposed scar drag model is that only two parameters are required to be determined before performing a simulation: M_{Σ}^e and C_s^I . Normally when one looks at the terrain topography with its geomorphological features, combining the measured rock mass and scar depths, one can already suggest a range for the M_{Σ}^e values. The subsequent task is to adjust the C_s^I value in a search grid for statistically and practically comparable numerical results with those of reality. For this purpose, one can even specify different M_{Σ}^e and C_s^I values for varying slope conditions. To test the sensitivity of our modelling results to M_{Σ}^e and C_s^I , we have performed another 4 groups of 5000 simulations varying M_{Σ}^e from 10 to 20 MN m⁻² and C_s^I from 1.0 to 2.0. The same post-processing procedure as shown in Fig. 13 has been conducted in order to compare the averaged rock dynamic quantities among the groups (Table 5). One can see that the model performance is quite consistent in the sense that rock tends to show a lower kinetic energy if one decreases M_{Σ}^e potentially increasing the maximum rock penetration depth or increases C_s^I directly enhancing the scarring drag force. This characteristic lays a solid foundation for the practical use of our rockfall energy dissipation model.

Conclusions and future work

Modelling rockfall energy dissipation due to impacts with scarring in soft compactable soils is the focus of this study. Instead of invoking effective restitution coefficients to model the rock energy loss at impacts, we propose to divide the rock-ground interaction into three separate processes involving a soft, deformable scarring layer and a hard, non-deformable rebound plane. The rock-ground impact process can then be divided into (1) a scarring phase, (2) a sliding phase on the rebound plane and (3) a rebounding phase in which the rock exits the scar. This model considers the plastic nature of the ground materials experiencing external collision and integrates both the fluid and solid behaviour of soil particles into the scarring drag force.

The scar drag model has been validated on both single impact and multi-impact, trajectory levels using induced 780-kg rockfall experiments performed at Chant Sura, Switzerland, in 2018. It can be concluded from our model validation that the new algorithm is able to capture to a large extent the energy loss of ground-impacting rocks. Regarding the model accuracy, the numerical results are in quantitatively good agreement with those obtained from the experiments, i.e. the rock dynamics such as translational and rotational speeds, jump height and jump length can be well captured through the energy dissipating processes. In particular, the performance of the model is exceptional when the rotational speed of rock at impact is relatively small. Regarding the model feasibility, the current scar drag model is easy to control in practice as there are only two physical parameters needed to be specified, namely the soil mechanical strength M_{Σ}^e and the scar drag coefficient due to soil compaction C_s^I . The simulated results are consistent because rockfall energy dissipation can be well managed by regulating M_{Σ}^e and C_s^I .

The above conclusions lay a solid foundation for applying our scar drag model on a wide extent of rockfall processes. The ongoing improvements of the computational algorithms focus on three aspects: (1) incorporating a rotational drag model in the scarring layer into the current non-smooth mechanics framework. This would help partially reducing the reducible errors discussed in this study; (2) collecting more experimental data for the

Table 5 Comparison of the averaged rock dynamic quantities obtained from 500 randomly selected 5-trajectory samples from the 5000 simulations with varying C_s^I and M_{Σ}^e values

C_s^I, M_{Σ}^e (MN m ⁻²)	Region	Translational speed (m s ⁻¹)	Rotational speed (° s ⁻¹)	Jump height (m)	Jump length (m)
1.5, 15	1	10.53 ± 0.43	922.93 ± 46.13	1.34 ± 0.10	4.09 ± 0.41
	2	17.44 ± 0.59	1745.29 ± 66.85	1.95 ± 0.17	9.92 ± 0.69
1.5, 10	1	10.27 ± 0.38	904.68 ± 41.30	1.30 ± 0.09	3.83 ± 0.39
	2	15.43 ± 0.58	1552.80 ± 65.63	1.67 ± 0.14	7.83 ± 0.59
1.5, 20	1	10.73 ± 0.43	938.32 ± 46.16	1.38 ± 0.11	4.28 ± 0.46
	2	18.63 ± 0.64	1852.61 ± 70.62	2.15 ± 0.21	11.31 ± 0.88
1.0, 15	1	10.76 ± 0.43	938.39 ± 47.28	1.37 ± 0.10	4.29 ± 0.43
	2	18.64 ± 0.63	1852.21 ± 69.29	2.14 ± 0.21	11.25 ± 0.87
2.0, 15	1	10.39 ± 0.38	915.40 ± 41.58	1.33 ± 0.09	3.97 ± 0.38
	2	16.37 ± 0.62	1647.01 ± 69.86	1.78 ± 0.15	8.73 ± 0.65

purpose of detailed model calibration. Currently, a series of rockfall experiments is being performed at Chant Sura using rocks of two shapes (flat and equant) ranging from 45 kg to 2.5 metric tons; (3) utilizing the rockfall energy dissipation model to terrains of various topographies and rocks spanning a greater range of shapes and masses. This is significant for natural hazards engineers who need representative values of soil mechanical strength and scar drag coefficient in order to apply the model in different geological settings.

References

- Albert I, Sample JG, Morss AJ, Rajagopalan S, Barabási AL, Schiffer P (2001) Granular drag on a discrete object: shape effects on jamming. *Phys Rev E* 64:061303
- Asteriou P, Tsiambaos G (2018) Effect of impact velocity, block mass and hardness on the coefficients of restitution for rockfall analysis. *Int J Rock Mech Min Sci* 106:41–50
- Asteriou P, Saroglou H, Tsiambaos G (2012) Geotechnical and kinematic parameters affecting the coefficients of restitution for rock fall analysis. *Int J Rock Mech Min Sci* 54:103–113
- Bartelt P, Gerber W, Christen M, Bühler Y (2016) Modeling rockfall trajectories with non-smooth contact/impact mechanics. In: Koboltschnig G (ed) *Proc., 13th Congress INTERPRAEVENT, International Research Society INTERPRAEVENT, Luzern, Switzerland*, pp 203–211
- Blasio FVD, Dattola G, Crosta GB (2018) Extremely energetic rockfalls. *J Geophys Res Earth Surf* 123:2392–2421
- Bourrier F, Berger F, Tardif P, Dorren L, Hungr O (2012) Rockfall rebound: comparison of detailed field experiments and alternative modelling approaches. *Earth Surf Process Landf* 37:656–665
- Caviezel A, Gerber W (2018) Brief communication: measuring rock decelerations and rotation changes during short-duration ground impacts. *Nat Hazards Earth Syst Sci* 18:3145–3151
- Caviezel A, Bühler Y, Lu G, Christen M, Bartelt P (2018a) Experimental validation of numerical rockfall trajectory models. In: Cardoso AS, Borges JL, Costa PA, Gomes AT, Marques JC, Vieira CS (eds) *Proc., 9th European Conference on Numerical Methods in Geotechnical Engineering, Faculty of Engineering, University of Porto, Taylor & Francis, Porto, Portugal*, pp 875–883
- Caviezel A, Schaffner M, Cavigelli L, Niklaus P, Bühler Y, Bartelt P, Magno M, Benini L (2018b) Design and evaluation of a low-power sensor device for induced rockfall experiments. *IEEE Trans Instrum Meas* 67:767–779
- Caviezel A, Demmel SE, Ringenbach A, Bühler Y, Lu G, Christen M, Dinneen CE, Eberhard LA, von Rickenbach D, Bartelt P (2019) Reconstruction of three-dimensional rockfall trajectories using remote sensing and rock-based accelerometers and gyroscopes. *Earth Surf Dyn* 7:199–210
- Christen M, Bühler Y, Bartelt P, Leine R, Glover J, Schweizer A, Graf C, McArdell BW, Gerber W, Deubelbeiss Y, Feistl T, Volkwein A (2012) Integral hazard management using a unified software environment: numerical simulation tool “ramms” for gravitational natural hazards. In: Koboltschnig G, Hübl J, Braun J (eds) *Proc., 12th Congress INTERPRAEVENT, International Research Society INTERPRAEVENT, Grenoble, France*, pp 77–86
- Corona C, Lopez-Saez J, Favillier A, Mainieri R, Eckert N, Trappmann D, Stoffel M, Bourrier F, Berger F (2017) Modeling rockfall frequency and bounce height from three-dimensional simulation process models and growth disturbances in submontane broadleaved trees. *Geomorphology* 281:66–77
- Dorren LKA (2016) Rockyfor3D (v5.2) revealed – transparent description of the complete 3D rockfall model. *ecorisQ paper* (www.ecorisq.org): 32p
- Effeindzourou A, Thoeni K, Giacomini A, Wendeler C (2017) Efficient discrete modelling of composite structures for rockfall protection. *Comput Geotech* 87:99–114
- Gang L, Hu XW, Du YJ, Fu JK, Mei XF (2018) A collision fragmentation model for predicting the distal reach of brittle fragmentable rock initiated from a cliff. *Bull Eng Geol Environ* 78:579–592
- Gao G, Meguid MA (2018) On the role of sphericity of falling rock clusters – insights from experimental and numerical investigations. *Landslides* 15:219–232
- Gerber W (2019) Naturgefahr Steinschlag: Erfahrungen und Erkenntnisse. WSL-Bericht, Birmensdorf
- Gischig VS, Hungr O, Mitchell A, Bourrier F (2015) Pierre3d: a 3d stochastic rockfall simulator based on random ground roughness and hyperbolic restitution factors. *Can Geotech J* 52:1360–1373
- Gratchev I, Saeidi S (2018) The effect of surface irregularities on a falling rock motion. *Geomech Geoen* 14:52–58
- Lambert S, Bourrier F, Toe D (2013) Improving three-dimensional rockfall trajectory simulation codes for assessing the efficiency of protective embankments. *Int J Rock Mech Min Sci* 60:26–36
- Leine RI, Schweizer A, Christen M, Glover J, Bartelt P, Gerber W (2014) Simulation of rockfall trajectories with consideration of rock shape. *Multibody Syst Dyn* 32:241–271
- Li LP, Lan HX (2015) Probabilistic modeling of rockfall trajectories: a review. *Bull Eng Geol Environ* 74:1163–1176
- Li XF, Li HB, Zhang QB, Jiang JL, Zhao J (2018) Dynamic fragmentation of rock material: characteristic size, fragment distribution and pulverization law. *Eng Fract Mech* 199:739–759
- Lu G, Third JR, Müller CR (2015) Discrete element models for non-spherical particle systems: from theoretical developments to applications. *Chem Eng Sci* 127:425–465
- Lu G, Caviezel A, Christen M, Bühler Y, Bartelt P (2018) Modelling rockfall dynamics using (convex) non-smooth mechanics. In: Cardoso AS, Borges JL, Costa PA, Gomes AT, Marques JC, Vieira CS (eds) *Proc., 9th European Conference on Numerical Methods in Geotechnical Engineering, Faculty of Engineering, University of Porto, Taylor & Francis, Porto, Portugal*, pp 575–583
- Macciotta R, Martin CD, Cruden DM (2015) Probabilistic estimation of rockfall height and kinetic energy based on a three-dimensional trajectory model and Monte Carlo simulation. *Landslides* 12:757–772
- Studer C, Leine RI, Glocker C (2008) Step size adjustment and extrapolation for time-stepping schemes in non-smooth dynamics. *Int J Numer Methods Eng* 76:1747–1781
- Thoeni K, Giacomini A, Lambert C, Sloan SW, Carter JP (2014) A 3d discrete element modelling approach for rockfall analysis with drapery systems. *Int J Rock Mech Min Sci* 68:107–119
- Toe D, Mentani A, Govoni L, Bourrier F, Gottardi G, Lambert S (2018) Introducing meta-models for a more efficient hazard mitigation strategy with rockfall protection barriers. *Rock Mech Rock Eng* 51:1097–1109
- Volkwein A, Schellenberg K, Labiouse V, Agliardi F, Berger F, Bourrier F, LKA D, Gerber W, Jaboyedoff M (2011) Rockfall characterisation and structural protection – a review. *Nat Hazards Earth Syst Sci* 11:2617–2651
- Volkwein A, Brügger L, Gees F, Gerber W, Krummenacher B, Kummer P, Lardon J, Sutter T (2018) Repetitive rockfall trajectory testing. *Geosciences* 8:88
- Wang YH, Jiang W, Cheng SG, Song PC, Mao C (2018) Effects of the impact angle on the coefficient of restitution in rockfall analysis based on a medium-scale laboratory test. *Nat Hazards Earth Syst Sci* 18:3045–3061
- Zhang YL, Liu ZB, Shi C, Shao JF (2018) Three-dimensional reconstruction of block shape irregularity and its effects on block impacts using an energy-based approach. *Rock Mech Rock Eng* 51:1173–1191

G. Lu · A. Caviezel · M. Christen · S. E. Demmel · A. Ringenbach · Y. Bühler · C. E. Dinneen · P. Bartelt

WSL Institute for Snow and Avalanche Research SLF,
Flüelastrasse 11, 7260, Davos Dorf, Switzerland
Email: guang.lu@slf.ch

W. Gerber

Swiss Federal Institute for Forest, Snow and Landscape Research WSL,
Zürcherstrasse 111, 8903, Birmensdorf, Switzerland